The Astrophysical Journal Letters, 959:L15 (10pp), 2023 December 20 https://doi.org/10.3847/2041-8213/ad0c54

Observing Planetesimal Formation under Streaming Instability in the Rings of HD 163296

F. Zagaria[1], C. J. Clarke[1], R. A. Booth[2], S. Facchini[3], and G. P. Rosotti[3]
[1] Institute of Astronomy, University of Cambridge, Madingley Road, Cambridge CB3 0HA, UK; fz258@cam.ac.uk
[2] School of Physics and Astronomy, University of Leeds, Leeds, LS2 9JT, UK
[3] Dipartimento di Fisica, Università degli Studi di Milano, Via Giovanni Celoria 16, I-20133 Milano, Italy
Received 2023 October 6; revised 2023 November 8; accepted 2023 November 14; published 2023 December 15

Abstract

We introduce a new technique to determine the gas turbulence and surface density in bright disk rings, under the assumption that dust growth is limited by turbulent fragmentation at the ring center. We benchmark this prescription in HD 163296, showing that our measurements are consistent with available turbulence upper limits and agree with independent estimates of the gas surface density within a factor of 2. We combine our results with literature measurements of the dust surface density and grain size to determine the dust-to-gas ratio and Stokes number in the 67 and 100 au rings. Our estimates suggest that particle clumping is taking place under the effect of streaming instability (SI) in the 100 au ring. Even though in the presence of external isotropic turbulence this process might be hindered, we provide evidence that turbulence is nonisotropic in both rings and likely originates from mechanisms (such as ambipolar diffusion) that could ease particle clumping under SI. Finally, we determine the mass accretion rate under the assumption that the disk is in steady state and turbulence regulates angular momentum transport. Our results are in tension with spectroscopic measurements and suggest that other mechanisms might be responsible for accretion, in qualitative agreement with the detection of a magnetocentrifugal wind in this system. Applying our method to larger samples can be used to statistically assess if SI is a viable mechanism to form planetesimals in bright rings.

Unified Astronomy Thesaurus concepts: CO line emission (262); Dust continuum emission (412); Gas-to-dust ratio (638); Planet formation (1241); Planetary cores (1247); Planetesimals (1259); Protoplanetary disks (1300); Submillimeter astronomy (1647)

1. Introduction

Planets form in gas- and dust-rich disks orbiting young stars. According to the core accretion model, this process takes place sequentially. At first, gentle collisions among micron-sized grains are expected to promote dust coagulation into millimeter- to centimeter-sized pebbles (e.g., Brauer et al. 2008; Birnstiel et al. 2010), in broad agreement with laboratory experiments (see Testi et al. 2014; Birnstiel et al. 2016) and (sub)millimeter continuum observations (e.g., Tazzari et al. 2016, 2021; Carrasco-González et al. 2019; Macías et al. 2021; Sierra et al. 2021; Guidi et al. 2022). However, larger grains are subject to larger relative particle velocities that can halt further dust coagulation (Brauer et al. 2008; Birnstiel et al. 2010) because of nonadhesive (bouncing; Zsom et al. 2010) or destructive (turbulent fragmentation; Ormel & Cuzzi 2007) collisions and radial drift (Weidenschilling 1977; Nakagawa et al. 1986). How pebbles overcome these growth barriers to form kilometer-sized bodies, the so-called planetesimals, is still a matter of debate.

The streaming instability (SI; Youdin & Goodman 2005; see also Simon et al. 2022; Lesur et al. 2023) is a promising solution to this conundrum. SI is a two-fluid resonant drag instability that arises from the differential rotation of gas and dust in the disk midplane (e.g., Squire & Hopkins 2020). In a cylindrical shear flow with a radially decreasing pressure gradient, gas rotates with sub-Keplerian velocity. Dust, instead, is not pressure-supported and orbits with Keplerian speed. Because of this azimuthal velocity difference, the gas drag reduces the angular momentum of solids that decouple from the background gas and drift radially inward. However, when dust backreaction on gas is strong enough, it increases the gas azimuthal velocity, reducing the dust drift efficiency (Johansen & Youdin 2007) and favoring the pileup of solids (Youdin & Johansen 2007). In the presence of dust overdensities, this mechanism can rapidly lead to strong particle concentration, creating narrow dust filaments dense enough to favor the collapse of self-gravitating particle clumps that will eventually form planetesimals (Johansen et al. 2007, 2009).

Among the other planetesimal formation mechanisms proposed in recent years (e.g., hierarchical coagulation models, such as porous growth or growth by mass transfer; see Johansen et al. 2014; Blum 2018; Drążkowska et al. 2023 and references therein), SI appears to be the most promising one because it is consistent with a number of solar system observations, such as the structure of comets (Blum et al. 2017), the prograde rotation of trans-Neptunian objects (Nesvorný et al. 2019), the formation of contact binaries in the cold classical Kuiper Belt (e.g., Arrokoth; McKinnon et al. 2020), and its absolute magnitude distribution (Kavelaars et al. 2021).

Shearing box simulations of nonlinear dust–gas interactions in vertically stratified disks revealed that particle clumping under SI is governed by three main parameters: (i) the local dust-to-gas surface density ratio,

$$Z = \Sigma_{\rm dust}/\Sigma_{\rm gas}, \quad (1)$$

where $\Sigma_{\rm gas}$ and $\Sigma_{\rm dust}$ are the gas and dust surface densities, which determines the efficiency of dust backreaction; (ii) the

particle Stokes number, St, which describes the degree of coupling between gas and dust; and (iii) the pressure support,

$$\Pi = \frac{\Delta v}{c_s} = -\frac{1}{2}\frac{c_s}{v_K}\frac{d\ln P}{d\ln R}, \quad (2)$$

which determines the relative azimuthal velocity between gas and dust. Here $\Delta v = v_K - v_\varphi$ is the gas azimuthal velocity (v_φ) deviation from Keplerian rotation (v_K), c_s is the locally isothermal sound speed, P is the gas pressure, and R is the disk radial coordinate. Recent studies (Carrera et al. 2015; Yang et al. 2017; Li & Youdin 2021) showed that, at a fixed value of Π, particle clumping under SI is favored when $\mathrm{St} \approx 0.1$, but it requires progressively larger dust-to-gas ratios for smaller values of St. Steeper pressure gradients are also expected to hinder particle clumping (Johansen et al. 2007; Bai & Stone 2010a; Sekiya & Onishi 2018).

Evidence that disks frequently display substructures in dust continuum emission (Andrews et al. 2018; Long et al. 2018; Andrews 2020) suggests that bright rings could be sweet spots for planetesimal formation under SI. Indeed, gaps are expected to halt radial drift, piling solids up in bright rings, where the dust-to-gas ratio might be locally strongly enhanced, favoring SI-driven particle clumping. This popular hypothesis is supported by evidence that (at least some) bright rings are pressure traps (Dullemond et al. 2018; Rosotti et al. 2020; Izquierdo et al. 2023) and was successfully invoked to explain the optical depth of DSHARP rings (Stammler et al. 2019).

Even though the conditions for particle clumping in pressure bumps were recently studied using vertically stratified shearing box simulations in a number of physical settings (Carrera et al. 2021, 2022; Carrera & Simon 2022; Xu & Bai 2022a), no direct method to observationally assess if SI-driven planetesimal formation is underway in bright disk rings has been identified yet. Scardoni et al. (2021) proposed that particle clumping under SI might have observable effects, reducing the disk optical depth and affecting the (sub)millimeter spectral index depending on the size and opacity of the particles forming clumps. They also showed that the presence of SI-driven dust accumulations is consistent with the optical properties of Lupus disks. A more direct way to assess if SI is a robust mechanism to form planetesimals in bright rings would be to compare their physical properties (i.e., Z, St) with the available thresholds for particle clumping (Carrera et al. 2015; Yang et al. 2017; Li & Youdin 2021). However, measurements of the gas surface density, which are precluded in most cases, are needed to estimate such quantities.

In this Letter, we present a new analysis technique that combines information on dust temperature, density, and grain size from multifrequency dust continuum observations with knowledge of the dust-to-gas coupling to measure the dust-to-gas ratio and Stokes number in the 67 and 100 au rings of HD 163296, under the assumption that dust growth is fragmentation-limited. In Section 2, we introduce our method and justify its application to HD 163296. In Sections 3 and 4, we present and discuss our results; finally, in Section 5, we draw our conclusions and consider future prospects.

2. Methods

In the hypothesis that particle fragmentation due to turbulent relative motions sets the maximum grain size at the ring center, we can write (Birnstiel et al. 2012)

$$a_{max} \equiv a_{frag} = 0.37\frac{2}{3\pi}\frac{\Sigma_{gas}}{\rho_s \alpha_{turb}}\left(\frac{u_{frag}}{c_s}\right)^2, \quad (3)$$

where ρ_s is the dust material density, u_{frag} is the velocity threshold for dust fragmentation, and α_{turb} regulates the turbulent collision velocity of dust particles (Ormel & Cuzzi 2007). The Stokes number of a compact particle with size a_{frag} near the disk midplane can be written in the Epstein regime as

$$\mathrm{St}_{frag} = \frac{\pi}{2}\frac{a_{frag}\rho_s}{\Sigma_{gas}} \rightarrow \frac{\mathrm{St}_{frag}}{\alpha_{turb}} = \frac{\pi}{2}\frac{a_{frag}\rho_s}{\Sigma_{gas}\alpha_{turb}}. \quad (4)$$

a_{frag} in Equation (3) and $\alpha_{turb}/\mathrm{St}_{frag}$ in Equation (4) scale with the ratio and product of Σ_{gas} and α_{turb}, respectively; thus, combining these expressions allows us to disentangle the two and write an expression for turbulent diffusivity

$$\alpha_{turb} = 0.35\frac{u_{frag}}{c_s}\left(\frac{\alpha_{turb}}{\mathrm{St}_{frag}}\right)^{1/2} \quad (5)$$

and gas surface density

$$\Sigma_{gas} = 2.85\frac{\pi}{2}\rho_s a_{frag}\frac{c_s}{u_{frag}}\left(\frac{\alpha_{turb}}{\mathrm{St}_{frag}}\right)^{1/2}. \quad (6)$$

These expressions show that Σ_{gas} and α_{turb} can be determined from two sets of parameters: (i) the maximum grain size (a_{max}) and the dust midplane temperature ($c_s \propto T^{1/2}$), which can be measured using high angular resolution multi-frequency dust continuum observations, and (ii) the gas-to-dust coupling ($\alpha_{turb}/\mathrm{St}_{frag}$, under the assumption that dust radial diffusivity, α_r, is regulated by gas turbulence, i.e., $\alpha_r = \alpha_{turb}$). This can be inferred from the dust and gas ring widths, the latter of which is derived from the gradient of the azimuthal velocity deviations from Keplerian rotation (Dullemond et al. 2018; Rosotti et al. 2020), measured from the rotation curve of bright emission lines observed at high spectral resolution.

3. Results

As a proof of concept, we computed Σ_{gas} and α_{turb} in the 67 and 100 au rings of HD 163296 (e.g., Isella et al. 2018), a 6 Myr old, 1.95 $M_\odot$ young stellar object (Wichittanakom et al. 2020) located 100.96 pc away (Gaia Collaboration et al. 2021) and among the best-studied in the (sub)millimeter. This is the only source with state-of-the-art CO emission line data (e.g., Teague et al. 2018, 2021; Izquierdo et al. 2022, 2023), where dust properties were measured using multifrequency Atacama Large Millimeter/submillimeter Array (ALMA) and Very Large Array (VLA) continuum observations (Guidi et al. 2022).

We used the dust-to-gas coupling estimated by Rosotti et al. (2020)[4] in combination with the temperature and grain size determined by Guidi et al. (2022). We adopted a dust material density $\rho_s = 2.076\ \mathrm{g\ cm^{-3}}$, since Guidi et al. (2022) assumed that the dust is composed of 60% amorphous silicates

[4] The slope of the gas azimuthal velocity deviation from Keplerian rotation induced by the ring ($\delta v_\varphi = v_\varphi/v_K - 1$) measured by Rosotti et al. (2020) using DSHARP data (Andrews et al. 2018) are broadly consistent with those we estimated from the rotation curve of Izquierdo et al. (2023) using higher spectral resolution MAPS data (Öberg 2021).

Table 1
Ring Parameters Constrained from Multifrequency Dust and Gas Kinematics Observations

(1)	α_r/St (2)	T (K) (3)	$\log(a_{\rm frag}/{\rm cm})$ (4)	$\alpha_{\rm turb} \times 10^4$ (5)	$\Sigma_{\rm gas}$ (g cm^{-2}) (6)	$\Sigma_{\rm dust}$ (g cm^{-2}) (7)	$Z \times 10^2$ (8)	${\rm St}_{\rm frag} \times 10^3$ (9)
R67	0.23 ± 0.03	21.94 ± 0.10	-1.88 ± 0.11	6.09 ± 0.40	16.11 ± 4.32	0.267 ± 0.002	1.66 ± 0.45	2.65 ± 0.17
R100	0.04 ± 0.01	12.83 ± 0.08	-1.90 ± 0.13	3.32 ± 0.42	4.98 ± 1.64	0.454 ± 0.012	9.13 ± 3.02	8.31 ± 1.04

Note. (1) Ring ID. (2) Dust-to-gas coupling (from Rosotti et al. 2020). (3) and (4) Dust temperature and maximum grain size (from Guidi et al. 2022). (5) Turbulent diffusivity. (6) Gas surface density. (7) Dust surface density (from Guidi et al. 2022). (8) Dust-to-gas ratio. (9) Stokes number.

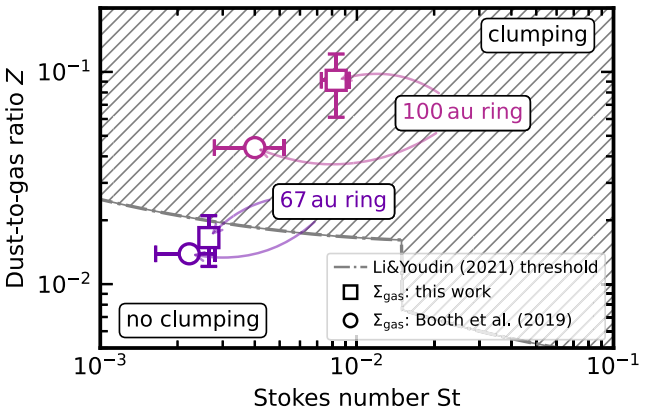

Figure 1. Dust-to-gas ratio and Stokes number of the 67 au (violet) and 100 au (purple) rings of HD 163296 plotted against the threshold for particle clumping in laminar disks ($\alpha_{\rm turb} = 0$) of Li & Youdin (2021). Squares display the values determined using the gas surface densities from Table 1, while circles show those computed from the gas mass measured by (Booth et al. 2019; see Table 2). The 100 au ring is prone to particle clumping under SI.

($Mg_{0.7}Fe_{0.3}SiO_3$; Dorschner et al. 1995), 15% amorphous carbon (Zubko et al. 1996), and 25% porosity by volume and a fragmentation velocity $u_{\rm frag} = 1\,{\rm m\,s^{-1}}$, motivated by recent laboratory experiments (Gundlach et al. 2018; Musiolik & Wurm 2019). Columns (1)–(6) of Table 1 summarize these parameters and our newly inferred $\Sigma_{\rm gas}$ and $\alpha_{\rm turb}$.

Independent literature measurements of these quantities can be used to benchmark our procedure. Flaherty et al. (2017) estimated the turbulent broadening of CO isotopologue and DCO^+ emission lines in the outer disk of HD 163296, showing that $\alpha_{\rm turb} < 3 \times 10^{-3}$, consistent with our results. Booth et al. (2019) forward modeled $^{13}C^{17}O$ emission in HD 163296 to constrain the total gas disk mass. Their fiducial gas surface density in the 67 and 100 au rings is reported in column (2) of Table 2 and shows a remarkable agreement with our estimates, falling within 1σ in R67 and 3σ in R100 (about a factor of 2 off).

We can use the gas surface density in Table 1 together with the grain size and dust surface density measured by Guidi et al. (2022) to determine Z and St from Equations (1) and (4). Our results are summarized in columns (7)–(9) of Table 1, while in columns (3) and (4) of Table 2, we report the values of Z and St computed using the gas surface densities of Booth et al. (2019) as a sanity check. Are these parameters consistent with SI forming particle clumps in the rings of HD 163296? In Figure 1, we show a comparison of the dust-to-gas ratio and Stokes number from Table 1 (squares) to Table 2 (circles) in R67 (violet) and R100 (purple) with the threshold for particle clumping under SI proposed by Li & Youdin (2021). The plot shows that SI-driven particle clumping is underway in the 100 au ring, as predicted by Stammler et al. (2019), both for the surface density from Equation (6) and the CO-based estimate of Booth et al. (2019).

Table 2
Same as Table 1, Using the CO-based Gas Surface Density of Booth et al. (2019)

(1)	$\Sigma_{\rm gas}$ (g cm^{-2}) (2)	$Z \times 10^2$ (3)	${\rm St}_{\rm frag} \times 10^3$ (4)
R67	19.20	1.39 ± 0.01	2.22 ± 0.58
R100	10.33	4.40 ± 0.12	4.00 ± 1.22

Note. (1) Ring ID. (2) Gas surface density. (3) Dust-to-gas ratio. (4) Stokes number.

4. Discussion

Hereafter, we discuss how the gas radial pressure gradient, disk turbulence, and particle size distribution can influence our results. We also comment on the assumptions we made in our derivation of the gas surface density and possible implications for disk evolution.

4.1. Pressure Support

The threshold for particle clumping by SI we adopted in Figure 1 was estimated with a suite of vertically stratified 2D shearing box simulations with $\Pi = 0.05$ (Li & Youdin 2021). However, since the 67 and 100 au rings of HD 163296 are pressure maxima (Rosotti et al. 2020), we should compare our results with the threshold for $\Pi \to 0$. In fact, Bai & Stone (2010a) showed that in this regime, particle clumping under SI requires lower values of Z. On the other hand, SI needs a nonnull pressure gradient to operate, otherwise no azimuthal velocity difference between dust and gas can sustain particle drift into local overdensities.[5]

Carrera et al. (2021, 2022) recently performed 3D shearing box simulations of SI-driven particle clumping in traffic jams (i.e., small-amplitude pressure bumps inducing local dust accumulations but not able to halt radial drift entirely). Surprisingly, they showed that solids with ${\rm St} = 0.012$ (similar to those in Table 1) never produce clumps for bump amplitudes as large as 50% (Carrera & Simon 2022), even though their local dust-to-gas ratio is well above the threshold proposed by Li & Youdin (2021). Instead, pressure bumps with amplitudes larger than 50% can lead to substantial particle clumping. In this case, however, SI is not needed to concentrate solids because the bump is strong enough to efficiently form planetesimals purely by gravitational instability (Carrera & Simon 2022).

[5] We stress, however, that even though SI cannot operate at the ring center, it could still take place in the wings.

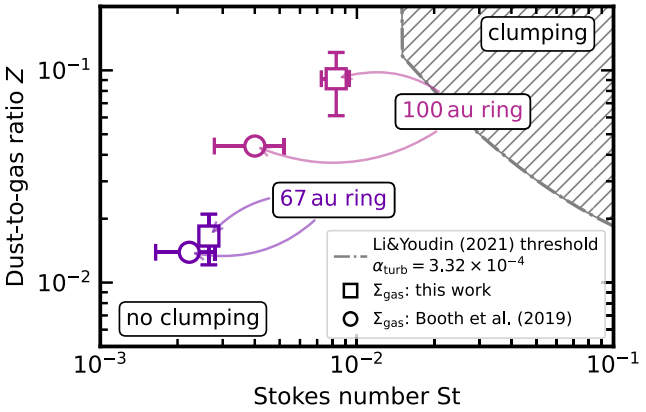

Figure 2. Same as Figure 1 but showing the threshold for particle clumping of Li & Youdin (2021) corrected for an isotropic turbulence level of $\alpha_{turb} = 3.32 \times 10^{-4}$. Both rings are stable against SI-driven particle clumping. However, we stress that turbulence is nonisotropic in R67 and R100, which leads to less stringent conditions for particle clumping.

Since Rosotti et al. (2020) showed that R67 and R100 are particle traps (corresponding to bump amplitudes larger than 70% in the simulations of Carrera & Simon 2022), the latter scenario seems to be closer to our case, suggesting that planetesimals could form through gravitational instability rather than SI in these rings. However, none of the previously cited simulations considered how turbulence could affect particle clumping. Instead, our results are based on the assumption that the 67 and 100 au rings of HD 163296 are in a steady-state balance between dust trapping and diffusion (see also Rosotti et al. 2020).

4.2. Turbulence

Turbulence, even at small levels, can be detrimental for particle clumping, reducing the midplane solid density and diffusing local dust enhancements. Although SI itself induces radial and vertical diffusivity (e.g., Johansen & Youdin 2007; Bai & Stone 2010b), the radial (α_r) and vertical (α_z) SI diffusion coefficients are $\alpha_z \lesssim \alpha_r \lesssim 10^{-6}$ for $\mathrm{St} \lesssim 10^{-2}$ (Li & Youdin 2021). Considering this value as the minimum diffusivity needed to interfere with SI, the turbulent levels we measured in the rings of HD 163296 (see Table 1) are high enough to affect the threshold for particle clumping in Figure 1.

To quantify the impact of turbulence on SI-driven particle clumping, Gole et al. (2020) performed 3D vertically stratified simulations including a forcing term in the gas momentum equation to generate an isotropic Kolmogorov-like turbulence. They proposed that turbulence primarily affects SI by increasing the thickness of the solid layer, changing the midplane dust-to-gas density ratio. Li & Youdin (2021) modified their threshold for particle clumping, including the effect of isotropic turbulence to reproduce the results of Gole et al. (2020). In Figure 2, this new threshold for $\alpha_{turb} = \alpha_{turb}(R = 100\,\mathrm{au})$ is plotted against the dust-to-gas ratio and Stokes number measured in R67 and R100. The plot shows that isotropic turbulence halts particle clumping under SI in both rings.

However, the turbulence implementation described by Gole et al. (2020) is idealized, since it does not take into account how magnetic fields could modify the properties of turbulence and how this is affected by particle overdensities. In fact, several works have argued that a more realistic treatment of external turbulence, such as nonideal magnetohydrodynamic (MHD) effects (e.g., ohmic dead zones; Yang et al. 2018) or the vertical shear instability (VSI; Schäfer et al. 2020), might even be beneficial for particle clumping, seeding SI in by large-scale effects, such as zonal flows or nonisotropic diffusivity.

Xu & Bai (2022b) recently performed vertically stratified 3D shearing box nonideal MHD simulations including the effects of ambipolar diffusion (AD). They found that the spontaneous formation of zonal flows promotes SI-driven particle clumping under less stringent conditions than in the laminar case, especially for shallower pressure gradients, showing that SI-driven planetesimal formation can take place with $\Pi = 0$ when AD is active. Additionally, Xu & Bai (2022a) found strong dust clumping in the case of pressure maxima with amplitudes of $\leqslant$50%. Although similar to those of Carrera & Simon (2022), these bumps achieved a quasi-steady-state balance between dust trapping and the turbulent diffusion generated by AD, as expected from our measurements (see Table 1). In the absence of dust feedback, nonideal MHD simulations with AD predict that vertical diffusion is larger than radial diffusion, $\alpha_z \gg \alpha_r$, because AD increases the eddy turnover time in the vertical direction (Xu & Bai 2022b). Instead, when dust backreaction is included, especially if particle clumping in pressure bumps takes place, it preferentially reduces the correlation time of vertical turbulent fluctuations, locally leading to $\alpha_z \ll \alpha_r$ (Xu & Bai 2022a).

To assess if SI-driven particle clumping in the presence of AD is a viable scenario for HD 163296, we adopted literature measurements of the dust-to-gas coupling in the vertical direction (Doi & Kataoka 2021; Liu et al. 2022) to determine the vertical diffusivity in the 67 and 100 au rings of HD 163296 using the Stokes numbers from Table 1. Our results are summarized in Table 3, and, when compared with our estimates of the radial diffusivity in Table 1, they suggest that turbulence is nonisotropic in both rings (see also Doi & Kataoka 2023).

In the 67 au ring, $\alpha_z \gg \alpha_r$, in qualitative agreement with the results of Xu & Bai (2022b) in the absence of significant particle loading in the midplane. We remark that VSI and nonideal MHD simulations with ohmic dead zones also predict a larger vertical than radial diffusion (Yang et al. 2018; Schäfer et al. 2020). However, we determined a cooling timescale ($t_{cool}\Omega_K \approx 6.5$) long enough for this ring to be stable against VSI. Additionally, we caveat that, when $\alpha_z \gg \alpha_r$, vertical turbulence might be the dominant mechanism in setting the grain size, increasing our measured α_{turb} and Σ_{gas} by a factor of 3. Nevertheless, since the estimate of a larger vertical

Table 3
Vertical Diffusivity in the 67 and 100 au Rings of HD 163296

(1)	α_z/St (2)	$\alpha_z \times 10^4$ (3)	α_z/St (4)	$\alpha_z \times 10^4$ (5)
R67	>2.4	>63.58	$2.3^{+2.5}_{-0.9}$	$60.93^{+66.35}_{-24.17}$
R100	<0.011	<0.91	$0.0038^{+0.02}_{-0.0013}$	$0.32^{+1.66}_{-0.12}$

Note. (1) Ring ID. (2) and (3) Dust-to-gas coupling (from Doi & Kataoka 2021) and vertical viscosity assuming the same St_{frag} from Table 1. (4) and (5) Same as in previous columns with the dust-to-gas coupling from Liu et al. (2022).

diffusivity in R67 follows from the inference of a puffed-up particle layer in this ring (Doi & Kataoka 2021), we considered the possibility that this high dust scale height can also be due to dust advection in a wind, as expected from AD models (e.g., Riols & Lesur 2018). Indeed, a molecular outflow was detected in HD 163296 and interpreted as a magnetocentrifugal wind (Booth et al. 2021). We determined the minimum wind mass-loss rate compatible with lofting 0.13 mm particles to the dust scale height inferred by Doi & Kataoka (2021) using the prescriptions of Giacalone et al. (2019, Equation (6)) and Booth & Clarke (2021, Equation (24)), making the conservative assumption that the wind base spans the range between 4 au (Booth et al. 2021) and 67 au (the ring location). In the latter case, we also assumed $z_{\rm IF} \approx H_{\rm IF}$ and a radially constant $\dot{\Sigma}$. Both prescriptions give similar values of $\dot{M}_{\rm loss} \approx 0.5 - 4 \times 10^{-6}\,M_\odot$ yr, broadly consistent with the mass-loss rate estimated by Booth et al. (2021). However, in this scenario, the thin scale height in R100 would imply a steep decrease in the mass-loss rate between 67 and 100 au. In the 100 au ring, instead, $\alpha_z \ll \alpha_r \approx 3.32 \times 10^{-4}$, in quantitative agreement with the results of Xu & Bai (2022a) for particle clumping in strong pressure bumps, supporting our hypothesis that SI is underway in this ring.

To summarize, isotropic turbulence is expected to halt particle clumping under SI. However, in the rings of HD 163296, turbulence is nonisotropic. Nonideal MHD simulations with AD show that the turbulence levels in R100 are consistent with SI-driven particle clumping. However, we caveat that these models only considered particles with St ≈ 0.1. To confirm that this process is underway in R100, new simulations with St ≈ 0.01 particles (similar to those in Table 1) need to be performed.

4.3. Particle Size Distribution

All of the previously mentioned simulations considered particle clumping in the monodisperse approximation. However, emission in the 67 and 100 au rings of HD 163296 is consistent with a power-law particle size distribution with exponent $q = 4$ (Guidi et al. 2022). Although the linear growth of SI in the polydisperse case remains under debate (Krapp et al. 2019), convergence to high growth rates can be achieved when either $\epsilon \gtrsim 1$ or $\mathrm{St}_{\rm max} \gtrsim 1$, especially for more top-heavy dust size distributions (Zhu & Yang 2021). Less idealized particle distributions motivated by fragmentation-coagulation models (Birnstiel et al. 2011) also seem to ease the linear growth of SI (McNally et al. 2021). Vertically stratified shearing box simulations with multiple particle species found that SI-driven particle clumping can take place (Bai & Stone 2010b; Rucska & Wadsley 2023). However, when $\max(\mathrm{St}) \lesssim 10^{-2}$, especially for flatter particle size distributions, more stringent (i.e., higher-Z) conditions than in the monodisperse case are required (Schaffer et al. 2021). Simulations considering how external turbulence and pressure bumps influence these results need to be performed for a proper comparison with our measurements.

4.4. Caveats on Dust Properties

As explained in Section 2, our results on the gas surface density and turbulence parameter are based on knowledge of the size, density, and temperature of dust that, in turn, depends on the particle composition assumed in the derivation (Guidi et al. 2022). In a recent paper, Jiang et al. (2023) estimated $\alpha_{\rm turb}$ and St radial profiles in HD 163296 extending to the entire disc our hypothesis that fragmentation limits the maximum grain size and adopting a dust-to-gas ratio of 10^{-2}, similar to what we found in R67. Nonetheless, their results ($\alpha_{\rm turb} \approx 10^{-4}$ and $\mathrm{St} \approx 4 \times 10^{-2}$) are slightly different from ours because they adopted the dust density and grain size estimated by Sierra et al. (2021) using DSHARP opacities (Birnstiel et al. 2018). Assessing how our results depend on dust composition self-consistently is beyond the aim of this Letter. However, in the Appendix, we provide a simple method to test how SI-driven particle clumping is affected by dust composition, under the assumption that the size, density, and temperature of dust accurately recover the gas surface density estimated by Booth et al. (2019), regardless of the assumed particle opacities. We show that both DSHARP compositions and mixtures including carbonaceous material are consistent with particle clumping under SI in the 100 au ring of HD 163296. Furthermore, we discuss how our results can be used to determine a fiducial dust composition.

4.5. Angular Momentum Transport

Under the assumption that turbulence regulates angular momentum transport in the disk, we can write the kinematic disk viscosity as $\nu = \alpha_{\rm SS} c_{\rm s}^2/\Omega_{\rm K}$ (Shakura & Sunyaev 1973), where $\alpha_{\rm SS} = \alpha_{\rm turb}$, and use a combination of Equations (5) and (6) to determine the steady-state mass accretion rate as

$$\dot{M}_{\rm acc,t} = 3\pi\nu\Sigma_{\rm gas} = \frac{3\pi^2}{2}\frac{c_{\rm s}^2}{\Omega_{\rm K}}\rho_{\rm s} a_{\rm frag}\left(\frac{\alpha_{\rm turb}}{\mathrm{St}_{\rm frag}}\right). \quad (7)$$

We notice that the predicted value does not depend on the fragmentation threshold velocity. Since turbulence in the 100 au ring might be affected by SI-driven particle clumping, we only determined the mass accretion rate in the 67 au ring, where $\dot{M}_{\rm acc,t} = (2.21 \pm 0.65) \times 10^{-9}\,M_\odot\ \mathrm{yr}^{-1}$. Observational measurements of the mass accretion rate of HD 163296 are debated. The most recent estimate (obs. date: 2013 June), based on Hα accretion luminosity, is $\log(\dot{M}_{\rm acc,obs}/M_\odot\ \mathrm{yr}) = -6.79^{+0.15}_{-0.16}$ (Wichittanakom et al. 2020). Instead, the closest previous epoch inference (obs. date: 2009 October), from the excess emission around the Balmer jump, suggests that $\log(\dot{M}_{\rm acc,obs}/M_\odot\ \mathrm{yr}) = -7.49^{+0.14}_{-0.30}$ (Fairlamb et al. 2015), in good agreement with the same epoch estimates based on the Brγ line luminosity (Grant et al. 2023). It is known that in HD 163296, the accretion rate experienced an abrupt increase of $\approx$1 dex about 20 yr ago (see Mendigutía et al. 2013 and Figure 8 of Ellerbroek et al. 2014). The measurement of Wichittanakom et al. (2020) is quantitatively consistent with this prolonged outburst phase (also notice that in steady state, it would imply that $\approx 0.97\,M_\odot$ of gas was accreted over the age of the system, so it is unreasonable to say that this accretion rate is maintained throughout the whole disk lifetime). Instead, the estimate of Fairlamb et al. (2015) is more consistent with the mass accretion rate measured in the quiescent phase. Therefore, we would be more prone to consider the latter as fitting our steady-state picture better.

In any case, both of these measurements are higher than our estimate of the turbulent mass accretion rate, implying that turbulence is not efficient enough to sustain accretion, in agreement with our hypothesis that AD might be in operation in the outer disk and consistent with the detection of a magnetocentrifugal wind in the system (Booth et al. 2021). We can combine our estimate of the turbulent angular momentum transport and the observed mass accretion rate to determine the efficiency of angular momentum transport due to MHD disk winds ($\alpha_{\rm DW}$; Suzuki et al. 2016; Tabone et al. 2022) as

$$\alpha_{\rm DW} \approx \alpha_{\rm SS}\frac{\dot{M}_{\rm acc,w}}{\dot{M}_{\rm acc,t}} = \alpha_{\rm SS}\left(\frac{\dot{M}_{\rm acc,obs}}{\dot{M}_{\rm acc,t}} - 1\right), \quad (8)$$

where $\dot{M}_{\rm acc,w}$ is the mass accretion rate due to MHD winds and the relative strength between the radial and vertical torque ($\psi = \alpha_{\rm DW}/\alpha_{\rm SS}$; Tabone et al. 2022). Our results give $\alpha_{\rm DW} = 4.41 \times 10^{-2}$, $\psi = 72.31$ using the $\dot{M}_{\rm acc,obs}$ of Wichittanakom et al. (2020) and $\alpha_{\rm DW} = 8.30 \times 10^{-3}$, $\psi = 13.63$ using the $\dot{M}_{\rm acc,obs}$ of Fairlamb et al. (2015).

Finally, we can relate $\alpha_{\rm DW}$ to the vertical and toroidal components of the magnetic field at the wind base, combining Equations (3) and (6) of Tabone et al. (2022) as

$$B_z B_\varphi|_{\rm base} = \frac{3\pi}{2}\frac{\Sigma_{\rm gas} c_s^2 \alpha_{\rm DW}}{R}. \quad (9)$$

Global nonideal MHD simulations including ohmic resistivity and AD showed that $B_z \approx B_{z,0}$ is vertically constant, while $B_\varphi \approx 20 B_{z,0}$ at the wind base, where $B_{z,0}$ is the vertically averaged vertical component of the magnetic field (Béthune et al. 2017). In R67, we determined $B_{z,0} = 0.36$ mG using the $\dot{M}_{\rm acc,obs}$ of Wichittanakom et al. (2020) and $B_{z,0} = 0.16$ mG using the $\dot{M}_{\rm acc,obs}$ of Fairlamb et al. (2015). These estimates are consistent with the upper limits on the vertical component of the magnetic field estimated in TW Hya (Vlemmings et al. 2019) and AS 209 (Harrison et al. 2021) from Zeeman splitting of the CN $J = 2 - 1$ line hyperfine component circular polarization observations. The corresponding plasma parameters (i.e., the ratio of thermal to magnetic pressure) are $\beta_0 = 8\pi P_0 B_{z,0}^{-2} = 1.75 \times 10^4$ and 8.78×10^4, respectively, where $P_0 \approx \Sigma_{\rm gas} c_s \Omega_{\rm K}/\sqrt{2\pi}$ is the midplane thermal pressure.

5. Summary and Future Prospects

We introduced a new technique to measure the turbulence and gas surface density in bright disk rings, under the assumption that grain growth is limited by fragmentation at the ring center. In the 67 and 100 au rings of HD 163296, the only source where this analysis can currently be carried out, our measurements are in remarkably good agreement with independent estimates. We then combined our results with literature measurements of the dust surface density and grain size to compute the dust-to-gas surface density ratio and Stokes number. By comparison with the threshold for particle clumping under SI proposed by Li & Youdin (2021), we found that the 100 au ring is undergoing planetesimal formation in the laminar case. Although external isotropic turbulence could halt particle clumping, we discussed how less idealized treatments of diffusivity, consistent with evidence of nonisotropic turbulence in the rings of HD 163296, might aid SI-driven particle clumping, especially in the 100 au ring. We proposed a consistent picture where AD is operating in the outer disk, seeding SI in and favoring particle clumping in the 100 au ring. This hypothesis is consistent with evidence that the turbulence is not strong enough to sustain accretion in the system, in agreement with the detection of an MHD disk wind.

The recent detection of a candidate protoplanet in the 94 au gap of HD 163296 (Teague et al. 2018; Izquierdo et al. 2022) suggests that a first generation of planetesimals already formed in this system. Indeed, with an age of 6 Myr (Wichittanakom et al. 2020), HD 163296 is a relatively old source. In this context, our result that SI is not operating in the 67 and 100 au rings, when external isotropic turbulence is considered, is not surprising and aligns with the hypothesis that planets must form early (Tychoniec et al. 2020). On the other hand, meteoritic records in the solar system indicate that planetesimal formation could take place through the whole disk lifetime (Lichtenberg et al. 2021). If the 100 au ring is unstable to SI, then it would likely be forming second-generation planetesimals. Simulations resolving particle clumps and studying their accretion history are needed to assess if these planetesimals will build planetary cores (the dust mass in the 100 au ring is 96^{+13}_{-16} $M_\oplus$, enough to form Jupiter's core with 20% efficiency; see Guidi et al. 2022) or a Kuiper Belt analog.

Applying our newly developed technique to a statistically significant sample spanning different disk and stellar properties (e.g., ring location, age, metallicity) could be promising to conclusively assess if SI is a viable mechanism to form planetesimals in bright rings. On the numerical side, more robust thresholds for particle clumping exploring a parameter space consistent with our measurements (pressure maxima in equilibrium between diffusion and drift with ${\rm St} \approx 0.01$ grains) are needed, but the real bottleneck is on the observational side, where our method requires (i) gas kinematics to measure the dust-to-gas coupling and (ii) high-resolution multifrequency observations to estimate the properties of dust. The exoALMA Large Program will significantly increase the number of disks with state-of-the-art CO emission observations, ideal for studying gas kinematics. However, the size, density, and temperature of dust have so far been successfully constrained only in a handful of sources, mainly because emission at wavelengths longer than 3 mm, which proved crucial in this analysis (e.g., Carrasco-González et al. 2019), was accessible only with VLA. We expect ALMA Band 1 (and ngVLA in the future) to significantly expand the sample of disks with well-constrained dust properties. Finally, disks where independent measurements of the gas surface density are also available can be used to further benchmark our analysis technique. Ideal sources are those targeted by the exoALMA Large Program, for gas surface density estimates based on self-gravity (Veronesi et al. 2021; Lodato et al. 2023), and AGE-PRO and DECO, for gas mass estimates based on rare CO isotopologues and N_2H^+ (Anderson et al. 2022; Trapman et al. 2022).

Acknowledgments

We are grateful to the referee for the insightful comments that helped to improve the quality of our manuscript and G. Guidi for sharing the dust density, temperature, and size radial profiles of HD 163296. F.Z. acknowledges support from STFC and Cambridge Trust for a PhD studentship. R.A.B. is supported by a University Research Fellowship. S.F. is funded by the European Union (ERC, UNVEIL, 101076613). G.R. is

funded by the European Union under the European Union's Horizon Europe Research & Innovation Programme No.1010 39651 (DiscEvol) and by the Fondazione Cariplo, grant No. 2022-1217. The views and opinions expressed are, however, those of the author(s) only and do not necessarily reflect those of the European Union or the European Research Council. Neither the European Union nor the granting authority can be held responsible for them. This project has received funding from the European Union's Horizon 2020 research and innovation program under Marie Sklodowska-Curie grant agreement No. 823823 (Dustbusters RISE project).

Facilities: ALMA, VLA.

Software: `JupyterNotebook` (Kluyver et al. 2016), `numpy` (Harris et al. 2020), `astropy` (Astropy Collaboration et al. 2022), `matplotlib` (Hunter 2007), `dsharp_opac` (Birnstiel et al. 2018).

Appendix
The Role of Dust Composition

Our results are based on literature estimates of the temperature, density, and size of dust that were obtained under the assumption of a specific solid composition (DIANA opacities; Woitke et al. 2016; Guidi et al. 2022). Here we discuss how our results for SI-driven particle clumping are affected by this assumption.

We can combine Equations (5) and (6) to write

$$\rho_s a_{\max} = \frac{2}{\pi}\Sigma_{\rm gas}\alpha_{\rm turb}\left(\frac{\alpha_{\rm turb}}{\rm St_{frag}}\right)^{-1}. \quad \text{(A1)}$$

Adopting the gas surface density estimate of Booth et al. (2019), the upper limit on turbulence of Flaherty et al. (2017), and the dust-to-gas coupling measured by Rosotti et al. (2020), we can determine upper limits for $\rho_s a_{\max}$ and the Stokes number (from Equation (4)). Our results are listed in columns (2) and (3) of Table 4, and we stress that they do not depend on dust composition (since the right-hand side of Equation (A1) does not).

Inverting Equation (5), we can determine the maximum dust fragmentation velocity threshold these upper limits correspond to,

$$u_{\rm frag} = 2.85\ \alpha_{\rm turb} c_s \left(\frac{\alpha_{\rm turb}}{\rm St_{frag}}\right)^{-1/2}, \quad \text{(A2)}$$

where we estimated the isothermal sound speed adopting the best-fit temperature profile that Guidi et al. (2022) self-consistently constrained, together with grain size and dust density. While this procedure might introduce some dependence of the dust temperature on the assumed composition, we consider the profile of Guidi et al. (2022) robust, since it agrees within a factor of 1.5 with independent temperature estimates based on the thermochemical models of Zhang et al. (2021) in both R67 and R100. As a consequence, we expect our inferred $\max(u_{\rm frag})$ values, listed in column (4) of Table 4, to also be insensitive to dust composition. We notice that $\max(u_{\rm frag}) < 10\ {\rm m\ s^{-1}}$, which is often adopted as a fragmentation velocity threshold for water ice–coated grains (Gundlach & Blum 2015). This upper limit is consistent with the results of Gundlach et al. (2018) and Musiolik & Wurm (2019) and our adopted fiducial $u_{\rm frag} = 1{\rm m\ s^{-1}}$.

Finally, from Equation (6),

$$\rho_s a_{\max} = 0.35\,\frac{2}{\pi}\Sigma_{\rm gas}\frac{u_{\rm frag}}{c_s}\left(\frac{\alpha_{\rm turb}}{\rm St_{frag}}\right)^{-1/2}, \quad \text{(A3)}$$

and under the hypothesis that $u_{\rm frag} = 1{\rm m\ s^{-1}}$ is the minimum possible fragmentation velocity threshold, we can determine lower limits for $\rho_s a_{\max}$ and the Stokes number. Our results are listed in columns (5) and (6) of Table 4, and considerations of their dependence on dust composition similar to those of Equation (A2) can be made.

We can use the upper and lower limits on $\rho_s a_{\max}$ in Table 4 to constrain the range of maximum grain sizes consistent with the gas surface density of Booth et al. (2019) and the upper limit on gas turbulence of Flaherty et al. (2017) for different dust compositions. These ranges are displayed in the top panel of Figure 3 for R67 (violet) and R100 (purple). We took into account the same dust mixtures considered in Appendix B of Birnstiel et al. (2018), and we refer to that paper for a detailed discussion of the materials involved. The $a_{\max}$ values we determined range from a few hundred microns to some millimeters, with the exception of only porous grains, whose maximum grain size can reach up to 1 cm. The dots and shaded regions of the same colors display the best-fit maximum grain sizes estimated by Guidi et al. (2022) and their 1σ uncertainty. Similar to what we noticed in Section 3, their results are compatible within 1σ in R67 and 3σ (a factor of 2) in R100, with the $\min(a_{\max})$ values based on the gas surface density of Booth et al. (2019) from Table 4.

We stress that the grain size ranges in Figure 3 only depend on the assumption that dust growth at the ring center is limited by turbulent fragmentation. Therefore, they can be used to discriminate between different dust compositions by comparison with the maximum grain sizes fitted self-consistently with dust density and temperature (e.g., as Guidi et al. 2022 did) for different dust mixtures. If the results of this analysis are not consistent with the intervals in Table 4, they will not be compatible with the gas surface density of Booth et al. (2019) or the turbulence upper limit of Flaherty et al. (2017), suggesting that they are less reliable. We postpone this analysis to a future paper.

We can make a step forward hypothesizing that emission is optically thin. In this case, the observed intensity can be approximated as $I_\nu \approx B_\nu(T)\kappa_\nu\Sigma_{\rm dust}$, where $B_\nu(T)$ is the Planck

Table 4
Upper and Lower Limits on $\rho_s a_{\max}$, Stokes Number, and Fragmentation Velocity Threshold from Equations (A1)–(A3)

	$\max(\rho_s a_{\max})$ (g cm^{-2})	$\max({\rm St})$	$\max(u_{\rm frag})$ (cm s^{-1})	$\min(\rho_s a_{\max})$ (g cm^{-2})	$\min({\rm St})$	$\min(u_{\rm frag})$ (cm s^{-1})
(1)	(2)	(3)	(4)	(5)	(6)	(7)
R67	1.59×10^{-1}	1.30×10^{-2}	4.92×10^{2}	3.24×10^{-2}	2.65×10^{-3}	10^{2}
R100	4.93×10^{-1}	7.50×10^{-2}	9.03×10^{2}	5.46×10^{-2}	8.31×10^{-3}	10^{2}

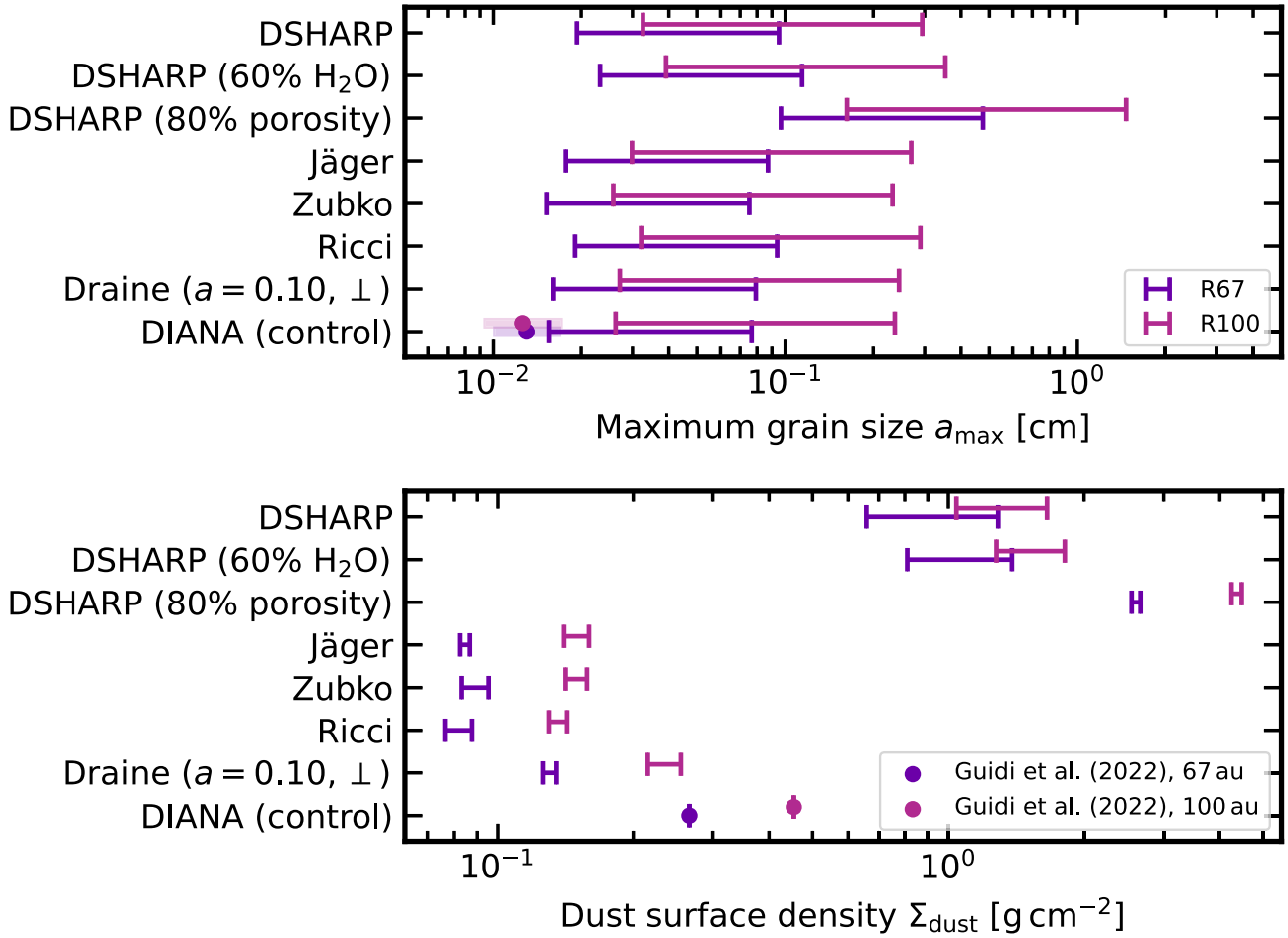

Figure 3. Top panel: maximum grain sizes compatible with the gas surface density estimate of Booth et al. (2019) and the upper limit on disk turbulence of Flaherty et al. (2017) for different dust compositions (see Appendix B of Birnstiel et al. 2018) in R67 (violet) and R100 (purple). The results (best-fit and 1σ spread) of Guidi et al. (2022) are shown as dots and shaded regions of the same color. Bottom panel: dust surface density estimates based on the best-fit of Guidi et al. (2022) in the optically thin limit.

function at frequency ν and temperature T, while κ_ν is the dust absorption opacity at frequency ν. Under the safe hypothesis that the temperature profile of Guidi et al. (2022) does not significantly change with dust composition (as discussed above), we can then compute the dust surface density for any solid composition in R67 and R100 as

$$\Sigma_{\rm dust} = \Sigma_{\rm dust,ref} \frac{\kappa_{\nu,\rm ref}(a_{\rm max,ref})}{\kappa_\nu(a_{\rm max})}, \tag{A4}$$

where the subscript "ref" stands for the reference composition and best-fit results of Guidi et al. (2022). We used the `dsharp_opac` package (Birnstiel et al. 2018) to generate 1.3 mm opacities for $q = 4$ (as inferred by Guidi et al. 2022 in both rings) and determined the upper and lower limits of $\Sigma_{\rm dust}$ for the minimum and maximum opacity within the range of maximum grain sizes determined from Table 4 (since the opacity profile is generally nonmonotonic, the minimum and maximum $\Sigma_{\rm dust}$ do not necessarily correspond the maximum and minimum $a_{\rm max}$).

Our results are displayed in the bottom panel of Figure 3. The different optical properties of each dust mixture determine a range of dust surface densities spanning a factor of 100. Taking the default DSHARP opacity ("DSHARP") as a reference, the 10 times lower opacity of porous DSHARP grains ("80% porosity") leads to much larger densities, while increasing the water content ("60% H_2O") has only a marginal effect on our final results. Instead, very different results are found when the organic materials typical of the DSHARP mixture are replaced by carbonaceous material, such as the "Jäger" (Jäger et al. 1998), "Zubko" (Zubko et al. 1996), "Ricci" (Ricci et al. 2010), and "Draine" (Draine 2003) compositions. Since they have much larger absorption opacities, they also lead to smaller dust densities. The results of Guidi et al. (2022) are intermediate between these two families.

We can use our dust surface density estimates from Equation (A4) and the gas surface density of Booth et al. (2019) to determine a range of dust-to-gas surface density ratios for each composition. Figure 4 shows a comparison of the threshold for particle clumping in the absence of external turbulence proposed by Li & Youdin (2021) and the (Z, St) ranges for different solid mixtures, color-coded by dust composition. It is clear that our result that SI-driven clumping is underway in R100 is common to all of the dust mixtures we tested. We also stress that it does not strongly depend on the $q \in \{2.5, 3.0, 3.5, 4.0\}$ and $\lambda/\mathrm{mm} \in \{1.3, 3.1, 9.1\}$ that we adopted to determine the dust densities. Instead, in R67, DSHARP opacities suggest that particle clumping is taking place, while carbonaceous grains would favor the nonclumping scenario.

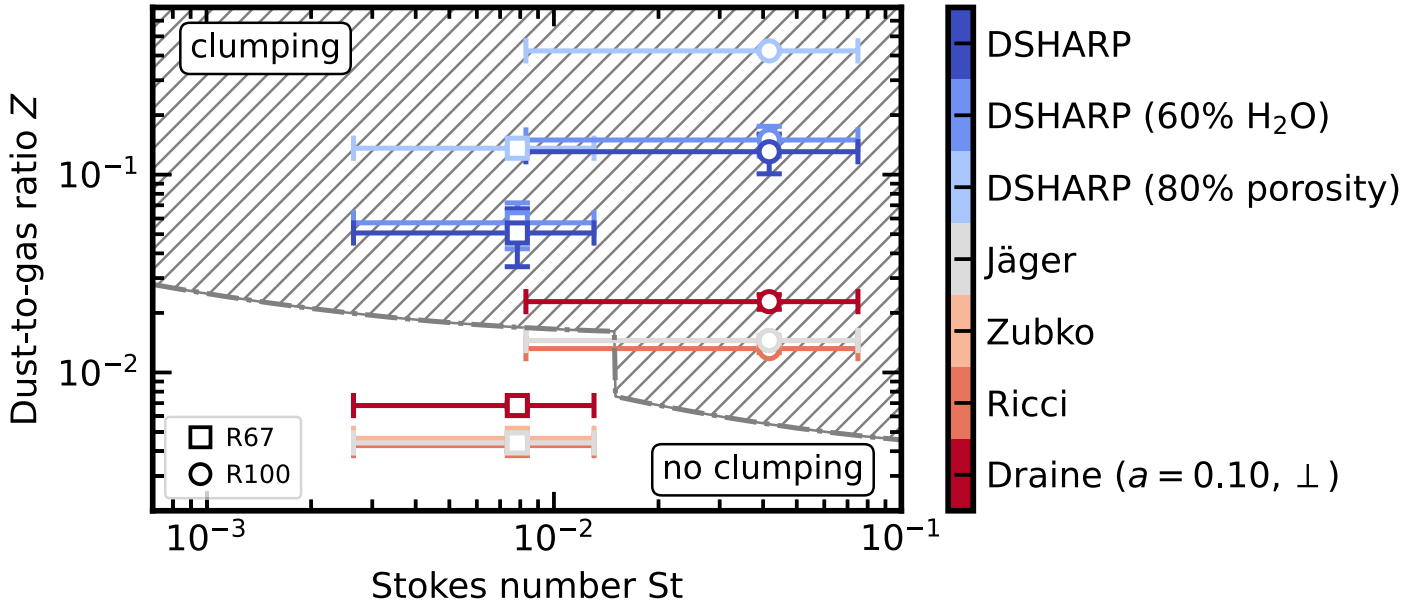

Figure 4. Comparison of the dust-to-gas surface density ratio and Stokes number for different compositions (color-coded) with the threshold for particle clumping of Li & Youdin (2021) in the laminar case. Our results that the 100 au ring is undergoing particle clumping under SI is consistent with different assumptions on grain mixtures.

ORCID iDs

F. Zagaria https://orcid.org/0000-0001-6417-7380
C. J. Clarke https://orcid.org/0000-0003-4288-0248
R. A. Booth https://orcid.org/0000-0002-0364-937X
S. Facchini https://orcid.org/0000-0003-4689-2684
G. P. Rosotti https://orcid.org/0000-0003-4853-5736

References

Anderson, D. E., Cleeves, L. I., Blake, G. A., et al. 2022, ApJ, 927, 229
Andrews, S. M. 2020, ARA&A, 58, 483
Andrews, S. M., Huang, J., Pérez, L. M., et al. 2018, ApJL, 869, L41
Astropy Collaboration, Price-Whelan, A. M., Lim, P. L., et al. 2022, ApJ, 935, 167
Bai, X.-N., & Stone, J. M. 2010a, ApJL, 722, L220
Bai, X.-N., & Stone, J. M. 2010b, ApJ, 722, 1437
Béthune, W., Lesur, G., & Ferreira, J. 2017, A&A, 600, A75
Birnstiel, T., Dullemond, C. P., & Brauer, F. 2010, A&A, 513, A79
Birnstiel, T., Dullemond, C. P., Zhu, Z., et al. 2018, ApJL, 869, L45
Birnstiel, T., Fang, M., & Johansen, A. 2016, SSRv, 205, 41
Birnstiel, T., Klahr, H., & Ercolano, B. 2012, A&A, 539, A148
Birnstiel, T., Ormel, C. W., & Dullemond, C. P. 2011, A&A, 525, A11
Blum, J. 2018, SSRv, 214, 52
Blum, J., Gundlach, B., Krause, M., et al. 2017, MNRAS, 469, S755
Booth, A. S., Tabone, B., Ilee, J. D., et al. 2021, ApJS, 257, 16
Booth, A. S., Walsh, C., Ilee, J. D., et al. 2019, ApJL, 882, L31
Booth, R. A., & Clarke, C. J. 2021, MNRAS, 502, 1569
Brauer, F., Dullemond, C. P., & Henning, T. 2008, A&A, 480, 859
CarrascoGonzález, C., Sierra, A., Flock, M., et al. 2019, ApJ, 883, 71
Carrera, D., Johansen, A., & Davies, M. B. 2015, A&A, 579, A43
Carrera, D., & Simon, J. B. 2022, ApJL, 933, L10
Carrera, D., Simon, J. B., Li, R., Kretke, K. A., & Klahr, H. 2021, AJ, 161, 96
Carrera, D., Thomas, A. J., Simon, J. B., et al. 2022, ApJ, 927, 52
Doi, K., & Kataoka, A. 2021, ApJ, 912, 164
Doi, K., & Kataoka, A. 2023, ApJ, 957, 11
Dorschner, J., Begemann, B., Henning, T., Jaeger, C., & Mutschke, H. 1995, A&A, 300, 503
Draine, B. T. 2003, ARA&A, 41, 241
Drążkowska, J., Bitsch, B., Lambrechts, M., et al. 2023, in ASP Conf. Ser. 534, Protostars and Planets VII, ed. S. Inutsuka et al. (San Francisco, CA: ASP), 717
Dullemond, C. P., Birnstiel, T., Huang, J., et al. 2018, ApJL, 869, L46
Ellerbroek, L. E., Podio, L., Dougados, C., et al. 2014, A&A, 563, A87
Fairlamb, J. R., Oudmaijer, R. D., Mendigutía, I., Ilee, J. D., & van den Ancker, M. E. 2015, MNRAS, 453, 976
Flaherty, K. M., Hughes, A. M., Rose, S. C., et al. 2017, ApJ, 843, 150
Gaia Collaboration, Brown, A. G. A., Vallenari, A., et al. 2021, A&A, 649, A1
Giacalone, S., Teitler, S., Königl, A., Krijt, S., & Ciesla, F. J. 2019, ApJ, 882, 33
Gole, D. A., Simon, J. B., Li, R., Youdin, A. N., & Armitage, P. J. 2020, ApJ, 904, 132
Grant, S. L., Stapper, L. M., Hogerheijde, M. R., et al. 2023, AJ, 166, 147
Guidi, G., Isella, A., Testi, L., et al. 2022, A&A, 664, A137
Gundlach, B., & Blum, J. 2015, ApJ, 798, 34
Gundlach, B., Schmidt, K. P., Kreuzig, C., et al. 2018, MNRAS, 479, 1273
Harris, C. R., Millman, K. J., van der Walt, S. J., et al. 2020, Natur, 585, 357
Harrison, R. E., Looney, L. W., Stephens, I. W., et al. 2021, ApJ, 908, 141
Hunter, J. D. 2007, CSE, 9, 90
Isella, A., Huang, J., Andrews, S. M., et al. 2018, ApJL, 869, L49
Izquierdo, A. F., Facchini, S., Rosotti, G. P., van Dishoeck, E. F., & Testi, L. 2022, ApJ, 928, 2
Izquierdo, A. F., Testi, L., Facchini, S., et al. 2023, A&A, 674, A113
Jäger, C., Mutschke, H., & Henning, T. 1998, A&A, 332, 291
Jiang, H., Macías, E., & Guerra-Alvarado, O. M. 2023, arXiv:2311.07775
Johansen, A., Blum, J., Tanaka, H., et al. 2014, in Protostars and Planets VI, ed. H. Beuther et al. (Tucson, AZ: Univ. Arizona Press), 547
Johansen, A., Oishi, J. S., Mac Low, M.-M., et al. 2007, Natur, 448, 1022
Johansen, A., & Youdin, A. 2007, ApJ, 662, 627
Johansen, A., Youdin, A., & Mac Low, M.-M. 2009, ApJL, 704, L75
Kavelaars, J. J., Petit, J.-M., Gladman, B., et al. 2021, ApJL, 920, L28
Kluyver, T., Ragan-Kelley, B., Pérez, F., et al. 2016, in Positioning and Power in Academic Publishing: Players, Agents and Agendas, ed. F. Loizides & B. Scmidt (Amsterdam: IOS Press)
Krapp, L., Benítez-Llambay, P., Gressel, O., & Pessah, M. E. 2019, ApJL, 878, L30
Lesur, G., Flock, M., Ercolano, B., et al. 2023, in ASP Conf. Ser. 534, Astronomical Society of the Pacific Conf. Ser., ed. S. Inutsuka et al. (San Francisco, CA: ASP), 465
Li, R., & Youdin, A. N. 2021, ApJ, 919, 107
Lichtenberg, T., Drążkowska, J., Schönbächler, M., Golabek, G. J., & Hands, T. O. 2021, Sci, 371, 365
Liu, Y., Bertrang, G. H. M., Flock, M., et al. 2022, SCPMA, 65, 129511
Lodato, G., Rampinelli, L., Viscardi, E., et al. 2023, MNRAS, 518, 4481
Long, F., Pinilla, P., Herczeg, G. J., et al. 2018, ApJ, 869, 17
Macías, E., Guerra-Alvarado, O., CarrascoGonzález, C., et al. 2021, A&A, 648, A33
McKinnon, W. B., Richardson, D. C., Marohnic, J. C., et al. 2020, Sci, 367, aay6620
McNally, C. P., Lovascio, F., & Paardekooper, S.-J. 2021, MNRAS, 502, 1469

Mendigutía, I., Brittain, S., Eiroa, C., et al. 2013, ApJ, 776, 44
Musiolik, G., & Wurm, G. 2019, ApJ, 873, 58
Nakagawa, Y., Sekiya, M., & Hayashi, C. 1986, Icar, 67, 375
Nesvorný, D., Li, R., Youdin, A. N., Simon, J. B., & Grundy, W. M. 2019, NatAs, 3, 808
Öberg, K. I., Guzmán, V. V., Walsh, C., et al. 2021, ApJS, 257, 1
Ormel, C. W., & Cuzzi, J. N. 2007, A&A, 466, 413
Ricci, L., Testi, L., Natta, A., et al. 2010, A&A, 512, A15
Riols, A., & Lesur, G. 2018, A&A, 617, A117
Rosotti, G. P., Teague, R., Dullemond, C., Booth, R. A., & Clarke, C. J. 2020, MNRAS, 495, 173
Rucska, J. J., & Wadsley, J. W. 2023, MNRAS, 526, 1757
Scardoni, C. E., Booth, R. A., & Clarke, C. J. 2021, MNRAS, 504, 1495
Schäfer, U., Johansen, A., & Banerjee, R. 2020, A&A, 635, A190
Schaffer, N., Johansen, A., & Lambrechts, M. 2021, A&A, 653, A14
Sekiya, M., & Onishi, I. K. 2018, ApJ, 860, 140
Shakura, N. I., & Sunyaev, R. A. 1973, A&A, 24, 337
Sierra, A., Pérez, L. M., Zhang, K., et al. 2021, ApJS, 257, 14
Simon, J. B., Blum, J., Birnstiel, T., & Nesvorný, D. 2022, arXiv:2212.04509
Squire, J., & Hopkins, P. F. 2020, MNRAS, 498, 1239
Stammler, S. M., Drążkowska, J., Birnstiel, T., et al. 2019, ApJL, 884, L5
Suzuki, T. K., Ogihara, M., Morbidelli, A., Crida, A., & Guillot, T. 2016, A&A, 596, A74
Tabone, B., Rosotti, G. P., Cridland, A. J., Armitage, P. J., & Lodato, G. 2022, MNRAS, 512, 2290
Tazzari, M., Clarke, C. J., Testi, L., et al. 2021, MNRAS, 506, 2804
Tazzari, M., Testi, L., Ercolano, B., et al. 2016, A&A, 588, A53
Teague, R., Bae, J., Aikawa, Y., et al. 2021, ApJS, 257, 18
Teague, R., Bae, J., Bergin, E. A., Birnstiel, T., & Foreman-Mackey, D. 2018, ApJL, 860, L12
Testi, L., Birnstiel, T., Ricci, L., et al. 2014, in Protostars and Planets VI, ed. H. Beuther et al. (Tucson, AZ: Univ. Arizona Press), 339
Trapman, L., Zhang, K., van't Hoff, M. L. R., Hogerheijde, M. R., & Bergin, E. A. 2022, ApJL, 926, L2
Tychoniec, Ł., Manara, C. F, Rosotti, G. P., et al. 2020, A&A, 640, A19
Veronesi, B., Paneque-Carreño, T., Lodato, G., et al. 2021, ApJL, 914, L27
Vlemmings, W. H. T., Lankhaar, B., Cazzoletti, P., et al. 2019, A&A, 624, L7
Weidenschilling, S. J. 1977, MNRAS, 180, 57
Wichittanakom, C., Oudmaijer, R. D., Fairlamb, J. R., et al. 2020, MNRAS, 493, 234
Woitke, P., Min, M., Pinte, C., et al. 2016, A&A, 586, A103
Xu, Z., & Bai, X.-N. 2022a, ApJL, 937, L4
Xu, Z., & Bai, X.-N. 2022b, ApJ, 924, 3
Yang, C.-C., Johansen, A., & Carrera, D. 2017, A&A, 606, A80
Yang, C.-C., Mac Low, M.-M., & Johansen, A. 2018, ApJ, 868, 27
Youdin, A., & Johansen, A. 2007, ApJ, 662, 613
Youdin, A. N., & Goodman, J. 2005, ApJ, 620, 459
Zhang, K., Booth, A. S., Law, C. J., et al. 2021, ApJS, 257, 5
Zhu, Z., & Yang, C.-C. 2021, MNRAS, 501, 467
Zsom, A., Ormel, C. W., Güttler, C., Blum, J., & Dullemond, C. P. 2010, A&A, 513, A57
Zubko, V. G., Mennella, V., Colangeli, L., & Bussoletti, E. 1996, MNRAS, 282, 1321